The Astrophysical Journal, 827:91 (7pp), 2016 August 20 doi:10.3847/0004-637X/827/2/91

STATISTICALLY DETERMINED DISPERSION RELATIONS OF MAGNETIC FIELD FLUCTUATIONS IN THE TERRESTRIAL FORESHOCK

B. Hnat[1], D. O'Connell[1], V. M. Nakariakov[1], and T. Sundberg[2]
[1] Centre for Fusion, Space and Astrophysics, University of Warwick, UK; B.Hnat@warwick.ac.uk
[2] School of Physics and Astronomy, Queen Mary University of London, UK
Received 2016 March 8; revised 2016 May 13; accepted 2016 May 17; published 2016 August 11

ABSTRACT

We obtain dispersion relations of magnetic field fluctuations for two crossings of the terrestrial foreshock by *Cluster* spacecraft. These crossings cover plasma conditions that differ significantly in their plasma β and in the density of the reflected ion beam, but not in the properties of the encountered ion population, both showing shell-like distribution function. Dispersion relations are reconstructed using two-point instantaneous wave number estimations from pairs of *Cluster* spacecraft. The accessible range of wave vectors, limited by the available spacecraft separations, extends to $\approx 2 \times 10^4$ km. Results show multiple branches of dispersion relations, associated with different powers of magnetic field fluctuations. We find that sunward propagating fast magnetosonic waves and beam resonant modes are dominant for the high plasma β interval with a dense beam, while the dispersions of the interval with low beam density include Alfvén and fast magnetosonic modes propagating sunward and anti-sunward.

Key words: shock waves – solar–terrestrial relations – turbulence

1. INTRODUCTION

The region upstream of the terrestrial bow shock provides a testbed for a large number of generic plasma processes, from Fermi acceleration (Bell 1978) and shock reformation (Leroy 1983) to a wide range of instabilities (Quest 1998). Due to the collisionless nature of the solar wind plasma, the kinetic energy of the upstream flow is redistributed by complex interactions of particles with fluctuations and through particle reflection (acceleration) at the shock (Fairfield 1969; Gosling et al. 1982). This leads to non-thermal velocity distribution functions upstream of the shock and these can become linearly unstable to small perturbations, resulting in large amplitude fluctuations in the magnetic field and other plasma parameters. Scattering and heating of ions by such fluctuations is of great importance for understanding the channels of momentum and energy exchange in the system. It is essential to keep in mind that, in the case of the terrestrial foreshock, the upstream flow is not laminar and that large amplitude, nearly harmonic fluctuations coexist with turbulent solar wind. Identification of frequencies where the turbulent energy transfer becomes dominant extends our understanding of wave–particle interaction processes.

On magnetohydrodynamic (MHD) scales, the unperturbed solar wind plasma at 1 AU shows correlations between velocity and magnetic field fluctuations characteristic of transverse Alfvén modes (Bruno & Carbone 2005). The phase coherence of these fluctuations is usually destroyed prior to their arrival at the foreshock, and only a single observation of pure Alfvénic mode at 1 AU has been reported (Wang et al. 2012) to date. Small density perturbations are also detected in the unperturbed solar wind and these are a mixture of the pressure-balanced structures of coronal origin and fast magnetosonic modes (Tu & Marsch 1994). The ion cyclotron waves, Alfvén waves with frequency near the ion cyclotron frequency and with the field aligned wave vector, have been suggested as a possible source of solar wind heating and acceleration, but unambiguous detection of these waves in the solar wind has been elusive; see, for example, Kasper et al. (2013). Upon entering the foreshock, the solar wind plasma interacts with the small population of reflected particles and this interaction modifies kinetic properties of the plasma and can lead to a significantly different dynamics.

Few classes of ion velocity distribution functions have been observed in the terrestrial foreshock (Gosling et al. 1978), and in the case of the quasi-parallel ($\Theta_{B,n} < 45^\circ$) bow shock these distributions have been associated with low-frequency electromagnetic fluctuations. Fast magnetosonic waves, traveling in the direction of the beam, are the most unstable modes destabilized by the cold and tenuous beam-like distributions, corresponding to ions traveling sunward and nearly parallel to the background magnetic field. For sufficiently dense and warm beams the destabilized fast wave can also propagate against the beam (Gary 1985). In addition to the beam-like distributions, there are also these of "diffuse" type (Gosling et al. 1978; Paschmann et al. 1981), which are nearly isotropic in the phase space and have large temperatures, sometimes exceeding 10 keV. Enhanced wave activity has been observed for these distributions, with both left- and right-handed modes competing in growth rates, in numerical simulations with different beam and plasma parameters (Sentman et al. 1981). We note the importance of minor ions, especially Helium He^{++}, which may resonate with the left-hand mode at low frequencies, where the power of fluctuations tends to be greater and provide an energy source for magnetoacoustic cyclotron instability (Dendy et al. 1994).

In principle, the range of frequencies supported by foreshock plasmas span many orders of magnitude, from ultra-low-frequency (ULF) waves at about 10^{-2} Hz to electron Langmuir waves at hundreds of kHz. A substantial experimental literature exists, where the dominant modes at low frequencies have been characterized in terms of their wave properties in different regions of the terrestrial foreshock (Hoppe & Russel 1983; Le 1991; Fazakerley et al. 1995; Eastwood et al. 2003). The focus on ULF waves is motivated by numerical simulations (Sentman et al. 1981; Winske & Leroy 1984; Gary et al. 1998), which established that, for realistic plasma parameters, beam-

Table 1
Physical and Spacecraft Parameters of the Investigated *Cluster* Intervals

	χ (km)	$\langle \boldsymbol{B} \rangle$ (nT), GSE	$\langle \boldsymbol{V}_{sw} \rangle$ (km s^{-1})	β	V_A (km s^{-1})	$\Theta_{V,B}$ deg	$\Theta_{\chi,V}$ deg	$\Theta_{\chi,B}$ deg	ω_{cp} (rad s^{-1})	r_p (km)
I1	70.5	(−6.9, 0.3, 1.3)	315.5	0.4	60.5	11	62	71	0.7	42.1
I2	82.3	(7.9, −3.9, 4.7)	406.6	3.2	93.0	147	31	141	1.0	177.5

Notes.
χ—distance between spacecrafts $C3 - C4$, $\langle \boldsymbol{B} \rangle$—magnetic field vector averaged over the interval, $\langle V_{sw} \rangle$—average solar wind speed, plasma $\beta \equiv 2\mu_0 n k_B T/b^2$, $V_A \equiv \langle B \rangle / \sqrt{\mu_0 \langle n \rangle m_i}$—average Alfvén speed, $\Theta_{V,B}$—angle between averaged solar wind velocity and the average magnetic field vector, $\Theta_{\chi,V}$—angle between averaged solar wind velocity and the average separation vector, $\Theta_{\chi,B}$—angle between the average magnetic field vector and the average separation vector, ω_{cp}—proton cyclotron frequency, r_p—proton gyro-radius calculated at ion temperature.

like distributions generate electromagnetic fluctuations in the low-frequency range, that is, below the ion cyclotron frequency. More recent work took into account other plasma parameters and their correlations with the magnetic field fluctuations, providing more unambiguous identification of MHD modes (Blanco-Cano & Schwartz 1997).

Multi-point *Cluster* observations, aided with the wave telescope technique (Pinçon & Lefeuvre 1991), provided estimates of the dispersion relations associated with the dominant modes in the low-frequency range and clearly demonstrated the existence of sunward propagating waves, broadly consistent with the ion beam instability as a generation mechanism (Narita et al. 2003). Given the multiple locations where unstable distributions may exist, the growth rates of relevant instabilities (of the order of 100 s) and the speed of the propagation (typically 50–100 km s^{-1}), one expects a continuous distribution of power for unstable modes (Sentman et al. 1981). In addition, nonlinear processes, for example, the decay instability of Alfvén waves or/and the modulation instability of the fast magnetosonic mode (Hollweg 1994), may lead to the redistribution of power.

Our purpose in this work is to quantify how fluctuating power is distributed among different quasi-coherent modes in two foreshock plasmas, which differ in their macroscopic parameters but have similar background ion distributions. This work extends previous multi-point studies by applying a statistical method (Beall et al. 1982) capable of detecting dispersion relations associated with different coexisting modes within the same set of fluctuations. Each time interval is treated as a set of independent shorter realizations, each contributing to a statistically generated dispersion relation represented as the cumulative power at each identified frequency and the corresponding wave number. We find that for anisotropic and dense beams the most energetic fluctuations are located on at the right-hand polarized mode and resonant ion beam branches of the dispersion relation. A smaller, but considerable, amount of power is also found in the left-hand polarized branch, which extends to large modules of wave number $kr_p \sim 0.75$ (where r_p is a proton Larmor radius). For the interval with a low-density ion beam the result is more complex; the dominant power at low frequencies is associated with slowly evolving and magnetic field aligned advected structures, but the remaining power is nearly equipartitioned between Alfvén and fast modes, both traveling sunwards and anti-sunwards.

2. DATA

The data set consists of two foreshock crossings, 2002 February 16 at 07:50–09:20 and 2002 February 20 at 16:56–17:56, hereafter referred to as I1 and I2, respectively. These foreshock crossings were selected based on the clear presence of wave modes in frequency spectra, in a form of distinct peaks, as well as for the small spacecraft separation of the spacecraft pair *C*3 and *C*4. We use magnetic field data from the FGM instrument (Balogh et al. 1997) with a sampling frequency of ∼22.5 Hz and spin resolution (4 s) CIS-HIA data (Réme et al. 2001) for plasma parameters. Table 1 presents a summary of the plasma parameters for both intervals. We note a large difference in ion plasma β for these intervals as well as a different direction of the main component of the magnetic field (GSE x direction)—for the interval I1 the magnetic field is directed toward the Earth, while interval I2 has magnetic field pointing sunwards. Both intervals has been studied before in the context of ULF waves (Lucek et al. 2004; Narita et al. 2004, 2003) and their possible impact on temperature anisotropy of the core ion population (Selzer et al. 2014).

Our analysis is undertaken for transverse fluctuations of the magnetic field expressed in minimum variance coordinates, which is equivalent to solving an eigenvalue problem for the measured magnetic field variance matrix. Calculated eigenvalues are proportional to the power along each principal axis and the minimum eigenvalue is associated with the axis parallel or anti-parallel to the direction of the wave vector. Transverse magnetic field fluctuations are these associated with the intermediate and the maximum eigenvalues. The ratio of the intermediate and minimum eigenvalues was ∼2.5–3.0, which is rather low, but we attribute it to the non-stationary character of these considerably long intervals. We note that the minimum variance direction is nearly identical on two spacecraft for both intervals, with the angle between the averaged magnetic field and the minimum variance direction from spacecraft *C*3 and *C*4 differing by a fraction of a degree.

Figure 1 presents a summary of the magnetic field data for the two intervals. These show typical values of the ion number density ($\langle n_p \rangle \sim 5$–$15\,\mathrm{cm}^{-3}$) of the solar wind and their bulk speed puts them in the slow solar wind category. Clear quasi-monochromatic wave trains are seen in panels (a) and (b), in which we plot snapshots of the transverse magnetic field component corresponding to the highest eigenvalue of minimum variance analysis. Two traces show data from spacecraft *C*3 (black) and *C*4 (red). These demonstrate that the observed temporal shift between the signals is never larger than a period of a wave. Panels (c) and (d) demonstrate that for sufficiently short subintervals a unique sense of polarization can be established in the spacecraft frame. While interval I2 shows fairly consistent left-hand polarization, interval I1 exhibits frequent changes from left- to right-hand polarization. The frequency spectra of transverse magnetic field components, shown in panel (e), reveal peaks at frequencies lower then the

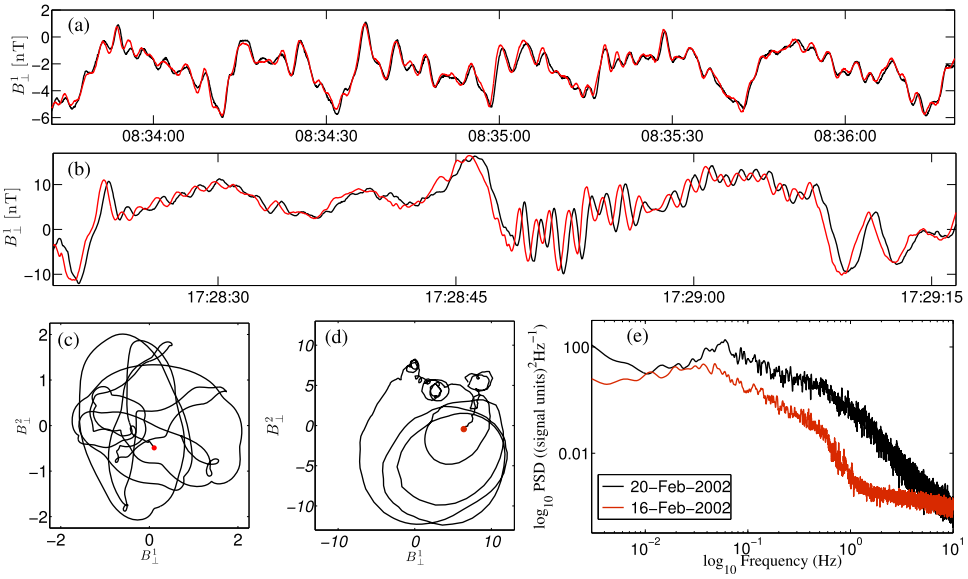

Figure 1. Magnetic field data summary for two time intervals. Panel (a): transverse magnetic field component associated with the largest eigenvalue of the minimum variance analysis for a section within I1 and for spacecraft *C*3 (black trace) and *C*4 (red trace). Panel (b): same as (a) for the interval I2. Panels (c) and (d): hodograms of the transverse magnetic field components for selected short subintervals in I1 and I2, respectively. Panel (e): power spectral density for $B_\perp^1$ component of interval I1 (red) and interval I2 (black).

proton gyro-frequency ($0.01 \leqslant \nu \leqslant 0.1$ Hz) and a broadband, power-law behavior at higher frequencies for both intervals. The proton cyclotron frequency in the plasma frame has been estimated for each interval at $\nu_{\rm cp}^{I1} \approx 0.11$ Hz and $\nu_{\rm cp}^{I2} \approx 0.16$ Hz, respectively, but a large Doppler shift put these in the range of 3–5 Hz in the spacecraft frame. Table 1 gives values of cyclotron frequencies in the plasma frame of reference.

3. METHODOLOGY

Transverse magnetic field components from spacecraft *C*3 and *C*4 are used to construct an estimate of the dispersion relation. We use a Fourier technique based on Beall's algorithm (Beall et al. 1982; Dudok de Wit et al. 1995; Balikhin et al. 1997; Hobara et al. 2007) designed for fixed probe pairs. Let $\boldsymbol{B}(\boldsymbol{r}, t)$ represent a zero-mean, stationary, homogeneous vector field, which can be represented as a superposition of plane waves, that is,

$$\boldsymbol{B}_t^i(\boldsymbol{r}, t) = \int_{-\infty}^{\infty} d\boldsymbol{k} \int_{-\infty}^{\infty} d\omega \tilde{\boldsymbol{B}}_t^i(\boldsymbol{k}, \omega) \exp[i(\boldsymbol{k}\cdot\boldsymbol{r} - \omega t)], \quad (1)$$

where B_t^i, with $i = 1, 2$, indicates transverse components obtained from the minimum variance analysis and the integrals are taken as the discrete sum of the measurements. The goal is to calculate an estimate of the dispersion relation, $\boldsymbol{k} = \boldsymbol{k}(\omega)$, which in the case of two probes located at $\boldsymbol{r}_1$ and $\boldsymbol{r}_2$, is given by a projection $k_\chi^p = \boldsymbol{k}(\omega)\cdot\boldsymbol{\chi}$, where $\boldsymbol{\chi} = \boldsymbol{r}_2 - \boldsymbol{r}_1$. Essentially, all required information is contained in the cross-spectral density, $H(\boldsymbol{\chi}, \omega)$, defined as:

$$H(\boldsymbol{\chi}, \omega) = \lim_{T\to\infty} \frac{1}{T} \langle \tilde{\boldsymbol{B}}_t^{i*}(\boldsymbol{r}_1, \omega) \tilde{\boldsymbol{B}}_t^i(\boldsymbol{r}_2, \omega) \rangle, \quad (2)$$

where T is the total time of the measurements and the angular brackets represent time averages. Expressing the complex quantity $H(\boldsymbol{\chi}, \omega)$ in polar representation allows the definition of the local estimated wave number k_χ^p, in terms of the phase

$$\Psi(\boldsymbol{\chi}, \omega) = \arctan[\mathrm{Im}(H(\boldsymbol{\chi}, \omega))/\mathrm{Re}(H(\boldsymbol{\chi}, \omega))],$$

$$k_\chi^p(\omega) = \frac{d}{d\boldsymbol{\chi}} \Psi(\boldsymbol{\chi}, \omega) \approx \frac{\Psi(\omega)}{\chi}. \quad (3)$$

The magnitude of the full wave vector is given by $k_\chi = k_\chi^p / \cos(\Theta_{\chi,k_\chi})$, where Θ_{χ,k_χ} is the angle between the separation vector $\boldsymbol{\chi}$ and the wave vector $\boldsymbol{k}_\chi$, which is estimated from the minimum variance analysis of a single spacecraft magnetic field. The definition of the projected wave number (3) introduces a natural ambiguity of $2j\pi$ ($j \in \mathbb{Z}$) and, in principle, the domain of k_χ^p spans an infinite number of negative and positive values. The incorrect identification of the relevant wave number interval may lead to the misinterpretation of plasma modes (see, for example, Balikhin et al. 1997; Dimmock et al. 2013). In practice, it is often clear from the visual inspection of the data which domain of k values is the relevant one and we will return to this issue in the next section.

In order to resolve a dispersion relation of multiple coexisting branches, it is necessary to calculate k_χ for an ensemble of data sets. Accordingly, for each interval in Table 1, the data is partitioned into N overlapping realizations of length T, chosen to include timescales of interest. The quantities given in (2) and (3) are then calculated for each realization. This yields the local joint wavenumber-frequency spectrum for each transverse component

$$\hat{S}(k_\chi, \omega) = \left\langle \frac{1}{2} (|\tilde{\boldsymbol{B}}_t^i(\boldsymbol{r}_1, \omega)|^2 + |\tilde{\boldsymbol{B}}_t^i(\boldsymbol{r}_2, \omega)|^2) \delta(k - k_\chi) \right\rangle, \quad (4)$$

where angular brackets now indicate an ensemble average. A histogram of discrete cells in k_χ and ω for $\hat{S}(k_\chi, \omega)$ is constructed, averaging over two transverse components to give the dispersion relation. Equation (4) converges to a real dispersion relation provided that (i) the plane wave approximation (1) is valid and (ii) $\boldsymbol{k}_\chi \cdot \boldsymbol{\chi} < 2\pi$. The quantity $\hat{S}(k_\chi, \omega)$ is then a discrete two-dimensional histogram of the

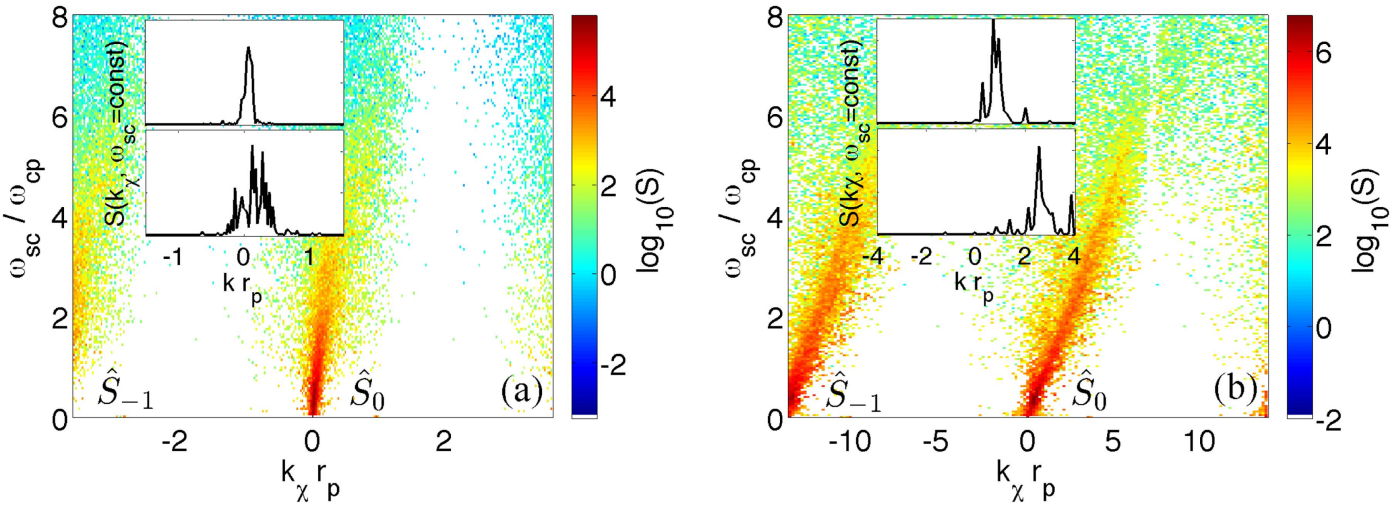

Figure 2. Histograms of normalized cumulative power on normalized frequency–wave number plane for interval I1 (a), and interval I2 (b). Symbols $\hat{S}_0$ and $\hat{S}_{-1}$ refer to wave numbers obtained from the phase difference Ψ and $\Psi - 2\pi$, respectively. Insets show cuts through $\hat{S}$ for two fixed frequencies; the top inset corresponds to $\omega_{sc} \approx 0.35\ \omega_{cp}$ and the bottom inset to $\omega_{sc} \approx 2.25\ \omega_{cp}$.

cumulative power on a (k_χ, ω) plane in the spacecraft reference frame.

In order to identify dispersion relations in the plasma rest frame, we apply the Doppler shift to (ω, k_χ) pairs which correspond to the maxima in $\hat{S}(\omega)$ at each frequency. In practice, we find three highest values of power, because some peaks may be over-resolved for a given number of bins in wave number and give the same Doppler shifted dispersion as the first maximum for some frequencies. The procedure is then as follows: we identify the three highest values of power in $\hat{S}(\omega)$ at each frequency, associate each frequency with its corresponding wave number k_χ, and Doppler shift these using the mean solar wind velocity, that is:

$$\omega_{pl} = \omega_{sc} - k_\chi |\langle V_{sw} \rangle| \cos(\Theta_{\boldsymbol{V},\boldsymbol{k}}), \quad (5)$$

where ω_{pl} and ω_{sc} are observed frequencies in plasma and spacecraft reference frame, respectively, $\langle V_{sw} \rangle$ is the solar wind speed averaged over the entire interval, and $\Theta_{\boldsymbol{V},\boldsymbol{k}}$ is the angle between the average solar wind velocity vector and the wave vector of the mode. Minimum variance analysis provides an estimate of the propagation direction of the wave with respect to magnetic field as a function of frequency. Since the angles between the magnetic field and the solar wind velocity as well as the magnetic field and the separation vector, χ, can be computed from data (see Table 1), the angle between the propagation direction (wave vector) and the solar wind velocity is also known. We have chosen the convention whereby ω is always positive and we therefore switch the sign of the wave number $k_\chi \to -k_\chi$ when Doppler shifted frequency $\omega_{pl} < 0$. Finally, we choose a sign of k_χ in GSE coordinate system, that is, $k_\chi > 0$ for waves traveling sunward and $k_\chi < 0$ for waves traveling toward the bow shock in the plasma rest frame.

The two-point-based technique presented above relies on a number of assumptions. For linear wave physics to be applicable, the wave amplitudes must be small. In the same time, these linear modes must have enough power to be clearly separated from the turbulent fluctuations. Small spacecraft separation is a key factor, since any nonlinear evolution of the signal in between the measurement points will diminish its cross-coherence.

4. RESULTS AND DISCUSSION

Figures 2 (a) and (b) show images of the cumulative power, $\hat{S}$ on the $(\omega_{sc}/\omega_{cp}, k_\chi r_p)$ plane, for intervals I1 and I2, respectively. Angular frequencies have been normalized by the proton cyclotron frequency, ω_{cp}, and the wave numbers by the proton gyro-radius, r_p, calculated using the perpendicular (with respect to magnetic field) ion temperature measured by CIS-HIA. The Nyquist frequency of the magnetic field measurements is 11 Hz, but we only show frequencies where some correlation of ω_{sc} and k_χ clearly exists. Beyond this range, turbulent fluctuations dominate, producing a random, broad signature, without any apparent features.

The repeated pattern of dispersion relations shown in Figure 2 has been obtained by subtracting and adding 2π to the k_χ values obtained from (3) and by artificially extending the range of these figures to $(-2\pi\chi, +2\pi\chi)$, normalized to the proton Larmor radius r_p. Two branches, labeled S_{-1} and S_0, are shown within this extended range to illustrate the $2j\pi$ ambiguity of the phase, as discussed in the previous section. Since the positive wave number is consistent with the observed signals, which propagate from spacecraft $C4$ to $C3$, and the visual inspection of the data does not support phase shifts larger than π, we base the following analysis on the cumulative power histogram, S_0, with wave numbers in the limit $(-\pi/\chi, \pi/\chi)$, which in SI units corresponds to wavelengths between $(-2.5, 2.5) \times 10^4$ m. This wave vector range has been divided into equally spaced 94 bins for I1 and 120 bins for I2. We note that the color scale used in the figure is that of $\log_{10}(\hat{S}_0)$. These plots were generated using ~100 strongly overlapping (~75% overlap) realizations, each 5 minutes long. The data for each realization has been linearly detrended and we subtracted the mean prior to obtaining the Fourier components.

Figure 2 demonstrates that a clear wave activity can be found when applying the method outlined in the previous section, but large Doppler shift strongly modifies the dispersion relations. Two insets shown in each panel of Figure 2 show cuts through $\hat{S}_0$ for two fixed frequencies; the top inset corresponds to $\omega_{sc} \approx$

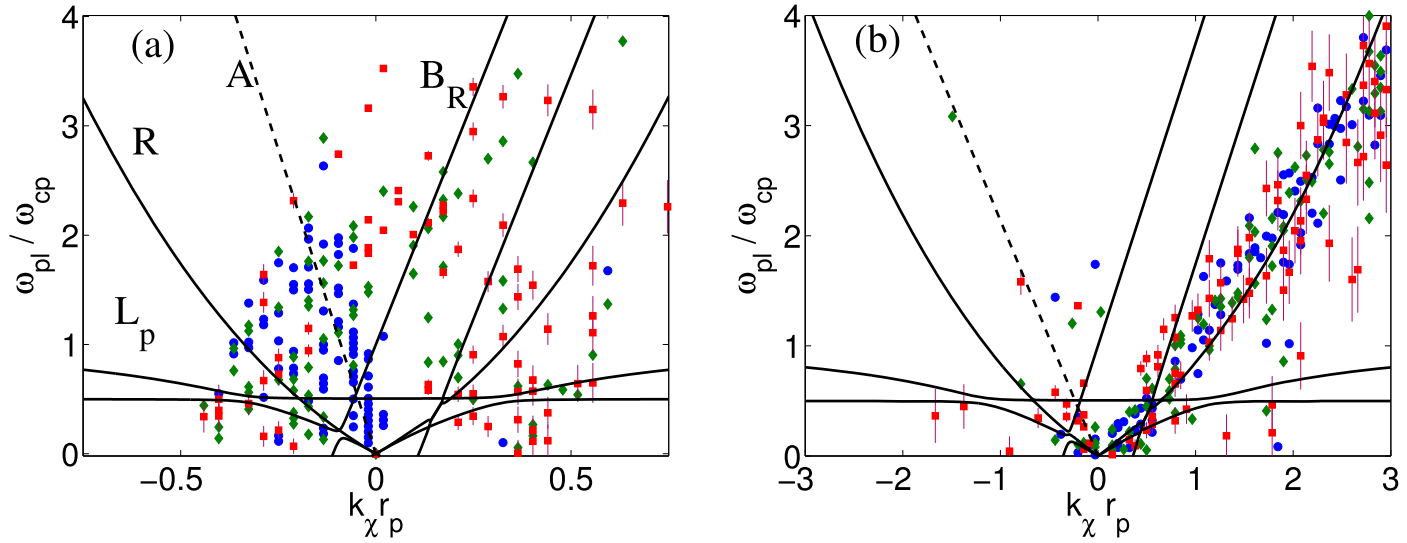

Figure 3. Doppler shifted estimates of dispersion relations obtained for interval I1 (a) and I2 (b) (solid points) and cold plasma dispersion relations as a function of wave vector amplitude (solid lines). Symbols correspond to different power maxima in $\hat{S}$ (see Figure 2): the first maximum (highest power for a given frequency) is shown as blue circles, the second maximum is shown as green diamonds, and the third as red squares. Errors are from the Doppler shift uncertainty. Labels of the solid lines indicate: *R*—fast magnetosonic mode, *A*—static structures advected by the solar wind, B_R—beam resonant modes, and L_p–Alfvén mode. The lines below the Alfvén branch correspond to He^{++} ion cyclotron mode.

$0.35\,\omega_{cp}$ and the bottom inset to $\omega_{sc} \approx 2.25\,\omega_{cp}$. These reveal the internal structure within the cumulative power histograms $\hat{S}_0$ with multiple peaks corresponding to different dispersion relations. As outlined before, we find the three highest local maxima in $\hat{S}_0$ and apply the Doppler shift to each identified $(\omega_{sc}/\omega_{cp}, k_\chi\, r_p)$ pair, as given in (5).

The minimum variance analysis provides the approximate angle of wave vectors with respect to the averaged magnetic field, which has values of $\Theta_{\boldsymbol{k},\boldsymbol{B}} \approx 55^\circ$ for the interval I1 and $\Theta_{\boldsymbol{k},\boldsymbol{B}} \approx 60^\circ$ for I2. We note that the minimum variance direction is nearly identical on two spacecraft for both intervals, with the angle between the averaged magnetic field and the minimum variance direction from spacecraft *C3* and *C4* differing by a fraction of a degree. The estimated angles are averages from spacecraft *C*3 and *C*4, which varied by approximately 1°. Using known angles between averaged vectors of the solar wind velocity $\boldsymbol{V}_{sw}$, the magnetic field $\boldsymbol{B}$, and the separation $\boldsymbol{\chi}$ (see Table 1), we obtain the magnitude of the wave vector and its angle with respect to the averaged solar wind velocity, $\Theta_{\boldsymbol{V},\boldsymbol{k}}$. This angle is ≈44° for I1 and ≈27° for I2. Then, applying Equation (5) we obtain the dispersion relation in the plasma frame of reference.

These dispersion relations, in normalized quantities, are shown in Figure 3 for each interval. Solid lines represent the cold plasma dispersion relations with massless electrons, background protons, background He^{++} ions, and a proton beam (Verscharen & Chandran 2013). We have used the beam propagation angle (w.r.t magnetic field vector) of 10° and beam velocity of 4.25 V_A for I1 and the angle of 30° and 5 V_A for I2, where V_A is the average Alfvén speed. The beam velocity was chosen based on the visual agreement of the theoretical dispersion curves with experimental observations. Different symbols used in the figure correspond to the power associated with the local maxima in $\hat{S}$, filled circles represent the highest power, and filled diamonds and squares correspond to the second and the third peak, respectively. The errors shown are due to the uncertainty in the Doppler shift with the turbulent velocity field and have been calculated based on the variance of the solar wind velocity.

There is a clear difference between the two intervals considered here. For the interval I1, the large Doppler shift moves the dispersion relation from $k_\chi r_p > 0$, as shown in Figure 2(a), to $k_\chi r_p < 0$. The most powerful fluctuations (filled circles) approximately satisfy the relation $\omega_{pl} \approx k_\chi \langle V_{sw} \rangle$ (dashed line), which implies that in the spacecraft frame these fluctuations propagated with velocities much larger than the Alfvén speed. Such unrealistically high velocities suggest that the majority of the large fluctuations are not associated with plain waves, but most likely represent field aligned structures advected past the spacecraft (see, for example, Alexandrova et al. 2006). Taking the relevant geometrical angles given in Table 1, we find that the apparent velocity read off the dispersion figure translates to approximately Alfvén speed when projected onto the magnetic field.

A small fraction of the most powerful fluctuations is also positioned near the fast magnetosonic and Alfvén branch of the dispersion curves for $k_\chi < 0$. These are waves traveling toward the bow shock and are most likely associated with the solar wind fluctuations. The points obtained from the secondary and the tertiary peak in power, shown as diamonds and squares, respectively, are equally distributed between fast magnetosonic and Alfvén modes propagating toward and away from the bow shock as well as the beam resonant mode. We have measured the ratio of power for the two dominant peaks, as a function of frequency, $PR(\omega) = \hat{S}(\omega)/\hat{S}_{max}(\omega)$. We found that this ratio shows a large increase around $\omega \approx 0.5\omega_{cp}$, so that $PR(\omega < 0.5\omega_{cp}) = 0.02$, while $PR(\omega > \omega_{cp}) = 0.6$. The largest k_χ value obtained for the sunward propagating Alfvén branch ($k_\chi > 0$) is approximately $k_\chi r_p = 0.5$, which is much larger than the numerically found value for the most unstable left- and right-hand polarized mode driven by cold beam (Gary 1985). Finally, we note a suggestive the presence of points near the ion cyclotron branch of helium, He^{++} for I1. This branch is difficult to study since the lower frequency modes require longer realizations to be considered. However, for the plasma

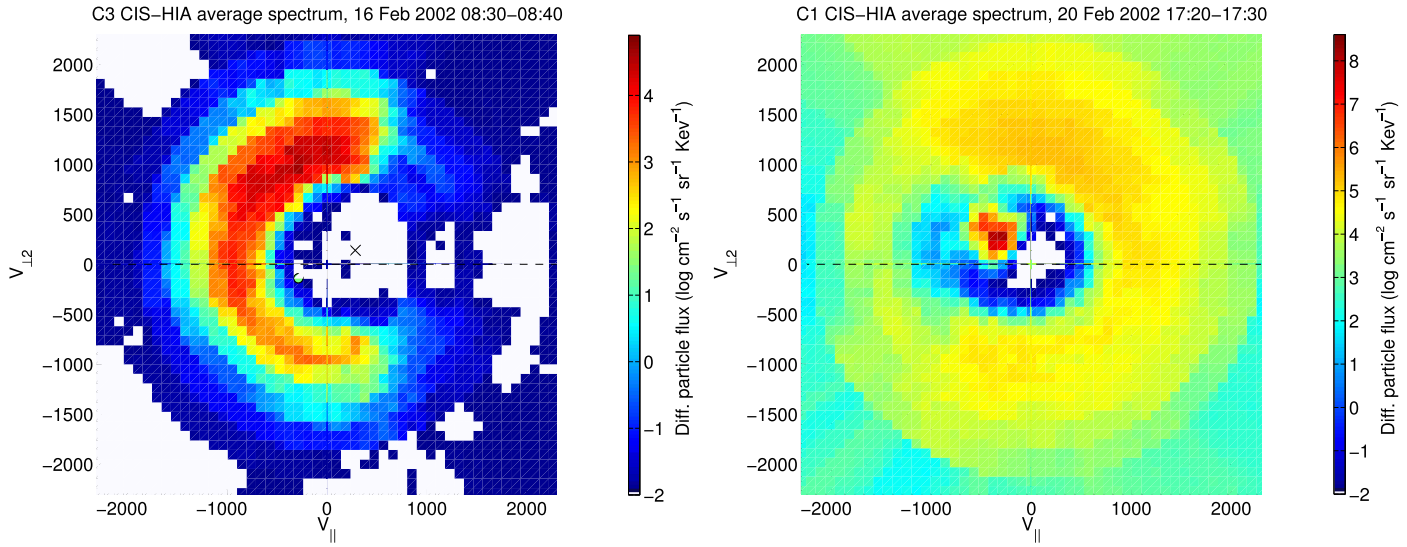

Figure 4. Differential particle flux in a magnetic field aligned coordinate system for the intervals I1 (left) and I2 (right). In the left panel, obtained from the HIA in the solar wind mode, the average location of the (excluded) solar wind has been marked with a cross.

that supports Bernstein modes, the minor ion resonance can contribute to magnetoacoustic cyclotron instability (Dendy et al. 1994).

We contrast this with the finding from interval I2, where all three most powerful modes are predominantly these of the right-hand polarized fast magnetosonic type, propagating sunward. We note the clustering of points along the straight solid line, marked B_R, which coincide with the low-frequency proton beam resonant modes. Similar to the previous interval, the secondary and tertiary populations appear to follow the He^{++} cyclotron branch for modes propagating sunward, some of which have $k_\chi\ r_p > 1$, which may indicate a large perpendicular wave number component. Finally, some residual amount of power is found in the modes propagating toward the bow shock. This result, while consistent with the previous analysis of this interval (Narita et al. 2003), supports numerical results which indicate that the unstable modes associated with the "diffused" ion population are both left- and right-hand polarized modes propagating sunward. We attribute residual power in the anti-sunward propagating modes with the solar wind population. We also note that the power in the tertiary peak is still very significant, approximately a half of the primary peak, for frequencies $\omega < 0.5\,\omega_{cp}$.

Having established signatures of multiple dispersion relations in each interval, we now examine proton distribution functions. Figure 4 shows HIA ion flux pitch angle distributions, observed within a ≈10 minute window in intervals I1 (top panel) and I2 (bottom panel), respectively. The CIS instruments were in the solar wind mode for interval I1, and in the magnetospheric mode during interval I2. In the magnetospheric mode, the instrument samples all angular directions and it is clear that the solar wind beam dominates the spectrum in this case. Accounting for this operational effect, both intervals show relatively typical shell-like ion distributions characteristic of the quasi-parallel foreshock. In both cases, the peak ion energies are few keV and the distributions have some angular asymmetries. The CIS-HIA spectra show the low level of the solar wind flux contamination for the interval I1, with the warm proton beam at energy of about 10 keV.

Ion beam density is one of the critical parameters affecting the type of modes that can be destabilized and the power associated with these fluctuations. We have calculated beam density by integrating phase space contributions from the CIS distributions excluding sections covering the solar wind beam, which are essentially these between ±45° and ±55° around the GSE x-axis (Réme et al. 2001). We find that the beam density for the intervals studied in here differs by one order of magnitude: the average number density for I1 is $n_b^{I1} \approx 0.025\ \mathrm{cm}^{-3}$, while for I2 it is much larger, $n_b^{I2} \approx 0.23\ \mathrm{cm}^{-3}$. Using the OMNI database, which provides approximate solar wind conditions upstream of the bow shock (http://omniweb.gsfc.nasa.gov), we find that the solar wind number density for both intervals differs by a factor of approximately 2: for I1 it is, $n_{sw}^{I1} \approx 7\ \mathrm{cm}^{-3}$ while for I2 it is $n_{sw}^{I2} \approx 14\ \mathrm{cm}^{-3}$.

5. CONCLUSIONS

We have identified multiple dispersion relations coexisting within the turbulent plasma for two different crossings of the terrestrial foreshock by *Cluster* spacecraft. These dispersions span beyond typically studied ULF waves in frequencies and in wave numbers, with the maximum angular frequency exceeding the proton gyro-frequency by a factor of up to four. Our methodology allows us to examine the distribution of power between different branches of the dispersion relation. Interval I1, while dominated by slowly evolving, field aligned structures advected by the solar wind, has a significant amount of power in Alfvén and fast magnetosonic waves propagating in sunward and anti-sunward directions. While for highly anisotropic beam temperatures ($T_{\perp,b} > T_{\parallel,b}$) the beam instability can generate ion cyclotron waves propagating parallel and anti-parallel to the magnetic field (Gary 1985), we must also admit a possibility that the anti-sunward propagating fluctuations are these embedded in the solar wind. Importantly, the presence of counter-propagating Alfvén modes may give rise to their nonlinear interaction. We have already highlighted a possibility of ion cyclotron modes of He^{++} and their importance for the magnetoacoustic cyclotron instability.

Interval I2 shows the dispersion relation dominated almost entirely by fast magnetosonic and resonant proton beam modes propagating away from the bow shock, indicating an instability of the cold ion beam, for which $\omega_{\rm pl} = k_{\|} v_b - \omega_{\rm cp}$, where v_b is the speed of the beam. This is in agreement with a previous study where the wave telescope technique has been used (Narita et al. 2003). In addition, extending previous results, we detect a significant amount of power in the Alfvén branch of the dispersion relation, propagating sunward. Some modes propagating anti-sunward are also present, close to both Alfvén and fast mode branches. The right-hand polarized waves of the interval I2 reach speeds of up to $v_{\rm ph}^R \approx 170\,{\rm km\,s^{-1}}$.

While the ion distribution functions have a similar form of an intermediate ring beam, for both intervals, the ion beam number density differs by an order of magnitude for the intervals. Interval I2 has much higher beam number density, which explains the dominant power in the magnetosonic modes, destabilized by the beam. In contrast, interval I1 shows an approximate equipartition of power between Alfvén and magnetosonic modes, when advected, slowly evolving structures are excluded. In this case, the fluctuations appear to be a complex admixture of the beam driven modes and Alfvénic modes embedded in the solar wind.

The quasi-parallel terrestrial foreshock region is one of the most complex plasma systems in which many linear plasma waves coexist with nonlinear waves and structures. It has been shown before that wave steepening of the large amplitude waves is a nonlinear dominant process for the ULF waves. Discrete wave packets may evolve according to the nonlinear Schrödinger equation (Zhu et al. 2008), when the cubic nonlinearity processes are present, and this can lead to wrong estimations of the propagation velocity (phases difference). These nonlinear interactions distribute the energy not only between different modes (Coca et al. 2001) but also between the bulk plasma and waves. The methodology applied in this paper does not take into account nonlinear interactions, and more detailed study is needed to measure the impact of the nonlinear waves and structures on the observed linear mode characteristics.

We acknowledge the CLUSTER team for data provision. B. H. was supported by the UK STFC (ST/I000720/1) and EU Marie Curie "Turboplasmas" funding.

REFERENCES

Alexandrova, O., Mangeney, A., Maksimovic, M., et al. 2006, JGR, 111, A12208
Balikhin, M. A., Dudok de Wit, T., Alleyne, H. St. C. K., et al. 1997, GeoRL, 24, 787
Balogh, A., Dunlop, M. W., Cowley, S., et al. 1997, SSRv, 79, 65
Beall, J. M., Kim, Y. C., & Powers, E. J. 1982, JAP, 53, 3933
Bell, A. R. 1978, MNRAS, 182, 147
Blanco-Cano, X., & Schwartz, S. J. 1997, AnGeo, 15, 273
Bruno, R., & Carbone, V. 2005, LRSP, 2, 4
Coca, D., Balikhin, M. A., Billings, S. A., Alleyne, H. S. C. K., & Dunlop, M. 2001, JGR, 106, 25005
Dendy, R. O., Lashmore-Davies, C. N., McClements, K. G., & Cottrell, G. A. 1994, PhPl, 1, 1918
Dimmock, A. P., Balikhin, M. A., Walker, S. N., & Pope, S. A. 2013, AnGeo, 31, 1387
Dudok de Wit, T., Krasnosel'skikh, V. V., Bale, S. D., et al. 1995, GeoRL, 22, 2653
Eastwood, J. P., Balogh, A., & Lucek, E. A. 2003, AnGeo, 21, 1457
Fairfield, D. H. 1969, JGR, 74, 3541
Fazakerley, A. N., Coates, A. J., & Dunlop, M. W. 1995, AdSpR, 15, 103
Gary, S. P. 1985, ApJ, 288, 342
Gary, S. P., Li, H., O'Rourke, S., & Winske, D. 1998, JGR, 103, 567
Gosling, J. T., Asbridge, J. R., Bame, S. J., Paschmann, G., & Sckopke, N. 1978, GeoRL, 5, 957
Gosling, J. T., Thomsen, M. F., Bame, S. J., et al. 1982, GeoRL, 9, 1333
Hobara, Y., Walker, S. N., Balikhin, M., et al. 2007, JGRD, 112, 202
Hollweg, J. V. 1994, JGR, 99, 23431
Hoppe, M. M., & Russel, C. T. 1983, JGR, 88, 2021
Kasper, J. C., Maruca, B. A., Stevens, M. L., & Zaslavsky, A. 2013, PhRvL, 110, 091102
Le, G. 1991, PhD thesis, Univ. California
Leroy, M. M. 1983, PhFl, 26, 2742
Lucek, E. A., Horbury, T. S., Balogh, A., Dandouras, I., & Réme, H. 2004, AnGeo, 22, 2309
Narita, Y., Glassmeier, K.-H., Schafer, S., et al. 2003, GeoRL, 30, 1710
Narita, Y., Glassmeier, K.-H., Schafer, S., et al. 2004, AnGeo, 22, 2315
Paschmann, G., Sckopke, N., Papamastorakis, I., et al. 1981, JGR, 86, 4355
Pinçon, J.-L., & Lefeuvre, F. 1991, JGR, 96, 1789
Quest, K. B. 1998, JGR, 101, 9649
Réme, H., Aoustin, H. C., Bosqued, J. M., et al. 2001, AnGeo, 19, 1303
Rosin, M. S., Schekochihin, A. A., Rinson, F., & Cowley, S. C. 2011, MNRAS, 413, 7
Selzer, L. A., Hnat, B., Osman, K. T., et al. 2014, ApJL, 788, L5
Sentman, D. D, Edmiston, J. P., & Frank, L. 1981, JGR, 86, 7487
Tu, C.-Y., & Marsch, E. 1994, JGR, 99, 21481
Verscharen, D., & Chandran, B. D. G. 2013, ApJ, 764, 88
Wang, X., He, J., Tu, C., et al. 2012, ApJ, 746, 147
Winske, D., & Leroy, M. M. 1984, JGR, 89, 2673
Zhu, D., Balikhin, M. A., Gedalin, M., et al. 2008, JGR, 113, A04221